Direct observation of conductive filament formation in Alq3 based organic resistive memories

Y. Busby,[1,a)] S. Nau,[2] S. Sax,[2] E. J. W. List-Kratochvil,[2,3] J. Novak,[4,b)] R. Banerjee,[4] F. Schreiber,[4] and J.-J. Pireaux[1]

[1]*Research Center in the Physics of Matter and Radiation (PMR), Laboratoire Interdisciplinaire de Spectroscopie Electronique (LISE), University of Namur, B-5000 Namur, Belgium*
[2]*NanoTecCenter Weiz Forschungsgesellschaft mbH, Franz-Pichler Straße 32, A-8160 Weiz, Austria*
[3]*Institute of Solid State Physics, Graz University of Technology, A-8010 Graz, Austria*
[4]*Institute of Applied Physics, Eberhard-Karls-Universität Tübingen, D-72076 Tübingen, Germany*

(Received 29 May 2015; accepted 3 August 2015; published online 19 August 2015)

This work explores resistive switching mechanisms in non-volatile organic memory devices based on tris(8-hydroxyquinolie)aluminum (Alq_3). Advanced characterization tools are applied to investigate metal diffusion in ITO/Alq_3/Ag memory device stacks leading to conductive filament formation. The morphology of Alq_3/Ag layers as a function of the metal evaporation conditions is studied by X-ray reflectivity, while depth profile analysis with X-ray photoelectron spectroscopy and time-of-flight secondary ion mass spectrometry is applied to characterize operational memory elements displaying reliable bistable current-voltage characteristics. 3D images of the distribution of silver inside the organic layer clearly point towards the existence of conductive filaments and allow for the identification of the initial filament formation and inactivation mechanisms during switching of the device. Initial filament formation is suggested to be driven by field assisted diffusion of silver from abundant structures formed during the top electrode evaporation, whereas thermochemical effects lead to local filament inactivation. © *2015 AIP Publishing LLC*.
[http://dx.doi.org/10.1063/1.4928622]

I. INTRODUCTION

Two terminal organic and hybrid resistive switching (RS) memories are promising candidates to develop routes towards high performance, easy-to-process, flexible, and non-volatile memories. The hybrid layer is typically fabricated by incorporating metal nanoparticles (NPs) in an organic matrix based on insulating or semiconducting polymers or small semiconducting molecules. Alternatively, a thin (discontinuous) intermediate metal layer is evaporated within the organic layer.[1,2] Hybrid RS devices based on metal NPs dispersed in tris(8-hydroxyquinoline) aluminum (Alq_3) have been widely reported in the literature, showing reliable switching properties, stable performances during prolonged cycling, and multi-bit storage capability making them suitable for different applications.[3] The RS mechanism in hybrid memories is still highly debated as it was associated to very different phenomena such as electrically induced conformational changes[4] and charge trapping in the NPs,[5–9] or to the formation of localized highly conductive paths, usually referred to as conductive filaments (CFs).[10–14] RS was recently shown to rely on CFs formation by modelling the electrical characteristics in a number of organic and hybrid memory structures. In particular, it was shown that metal/Alq_3/metal devices behave very similar as compared to hybrid devices based on Alq_3 containing metallic intermediate layers.[15–19] As compared to hybrid devices in organic devices, CFs are thought to form by metal diffusion during an electroforming step, after which bistability is typically observed.[20] While in crystalline organic semiconductors metal diffusion was correlated to the organic layer morphology and the metal deposition conditions,[21–25] in amorphous organic layers, such as Alq_3, metal diffusion has been rarely investigated.[26] The scarce analytical characterization, together with the rare studies on structural and/or compositional changes occurring during memory operation,[27] is probably at the origin of misinterpretations concerning the RS mechanism. Recent experiments with techniques such as conducting atomic force microscopy (AFM)[28,29] and transmission electron microscopy (TEM)[30–33] have succeeded in showing the presence of CFs. However, these challenging and time consuming experiments do not provide access to crucial information such as the spatial distribution of CFs, their composition, section, and dynamics during memory operation. For well-established inorganic resistive memories, CFs have been experimentally characterized[34–36] and are known to form by the field induced migration of metals or oxygen.[37] In ITO/Alq_3/Al memory devices, CFs were suggested to grow from metal nano-tips formed during the top electrode deposition;[19] however, no experimental evidence has been provided so far.

This work is dedicated to the investigation of metal diffusion and CF formation in Alq_3 based memories. The morphology and structural properties of hybrid Alq_3/Ag layers are characterized by X-ray reflectivity (XRR) as a function of the metal evaporation conditions. As-deposited and electrically cycled ITO/Alq_3/Ag memory elements, displaying reliable switching properties, are characterized with X-ray photoelectron spectroscopy (XPS) depth profiling and 3D

[a)]Electronic mail: yan.busby@unamur.be
[b)]Present address: Central European Institute of Technology, Masaryk University, Kamenice 5, CZ-62500 Brno, Czech Republic.

 © 2015 AIP Publishing LLC

[This article is copyrighted as indicated in the article. Reuse of AIP content is subject to the terms at: http://scitation.aip.org/termsconditions. Downloaded to] IP: 134.2.182.197 On: Mon, 24 Aug 2015 09:08:18

imaging with dual beam time-of-flight secondary ions mass spectrometry (ToF-SIMS) to investigate metal diffusion and CF formation.[38,39] ToF-SIMS analysis is performed with low energy $Cs^{(+)}$ ions which ensure low radiation damages and high ionization yields in negative polarity mode. Moreover, sputtering with $Cs^{(+)}$ ions has been shown to inhibit cross-linking by radical extinction, and convenient sputtering rates are obtained on both metals and organic layers.[40] The results clearly indicate the presence of CFs and allow for the interpretation of their evolution during memory operation.

II. EXPERIMENTAL

A. XRR measurements

X-ray specular reflectivity (XRR) is applied to study the surface and interface morphology on $Si/SiO_x/Alq_3/Ag$ hybrid samples. A systematic study has been carried by depositing by thermal evaporation a 15 nm thick silver layer on the top of Alq_3 at deposition rates ranging from $R_1 = 0.2$ Å/s (sample S1) to $R_2 = 10$ Å/s (sample S2). Additionally, a reference measurement is carried on the bare Alq_3 layer (sample S3). The XRR data are acquired on a GE XRD 3003TT diffractometer using Cu Kα1 radiation ($\lambda = 0.151$ nm) and are simulated by a three-layers model in *Parratt* formalism (*GenX* software[41]). The electron density and roughness of the underlying SiO_x layer are evaluated on a measurement on the bare substrate ($\rho_{SiOx} = 0.675$ Å^{-3} and $\sigma_{SiOx} = 0.20 \pm 0.02$ nm).

B. Device fabrication and testing

Glass/ITO substrates are cleaned in class 6 clean room using standard protocol ensuring a final roughness (Rq) <2 nm; then a 300 nm thick Alq_3 layer is UHV evaporated at 0.1 nm/s, and finally a $500 \times 500\ \mu m^2$ silver top electrode is thermally evaporated *in-situ* through a shadow mask at a rate of 1 nm/s. Electrical measurements are performed with an *Agilent B*1500*A* Parameter Analyzer at room temperature, in a glove box with controlled argon atmosphere ($O_2 < 1$ ppm and $H_2O < 1$ ppm). I-V scans are made by biasing the top electrode and measuring the current with a sweep rate of 200 ms and voltage steps of 0.1 V. Reliable switching was obtained after a short forming procedure by repeated cycling of the device, or alternatively, in the application of voltage pulses (>15 V) in the milliseconds range.

C. Depth profile analyses

Memory devices are depth profiled with XPS (*ESCALAB* 250*Xi* spectrometer by Thermo Scientific) to quantify the metal content and evaluate its vertical distribution within the organic layer. Depth profiles are built by alternating ion beam sputtering with 1 keV $Ar^{(+)}$ and XPS high resolution analysis with a $300 \times 300\ \mu m^2$ monochromatic X-ray beam centered in the sputtering area. Profiles showing the elemental composition (atomic percentage, at. %) as a function of the sputtering time (s) are converted into the more practical composition *vs* depth (nm) by successively measuring the crater depth with a stylus profilometer (*Dektak*). Memory elements set in different resistance states have been analyzed with ToF-SIMS 3D chemical imaging with a dual beam *TOF-SIMS IV* (IONTOF). 3D images are generated by alternating 2D imaging with $Bi_3^{(+)}$ beam at 25 keV and sputtering with low energy (500 eV) $Cs^{(+)}$ ions in a so-called non-interlaced mode. The analysis is performed on $100 \times 100\ \mu m^2$ area, with an in-plane resolution of about 1 μm, an in-depth resolution of about 1 nm, and a mass resolution of $M/\Delta M \sim 5000$.

III. RESULTS AND DISCUSSION

A. Characterization of Alq3/Ag hybrid layers

XRR analysis is carried to study the surface and interface morphology of $Si/SiO_x/Alq_3/Ag$ hybrid layers. The main results are shown in Figure 1(a) where the signal intensity is displayed as a function of the momentum transfer perpendicular to the sample surface (q_z); both high (see the inset) and low frequency oscillations can be identified, resulting, respectively, from the Alq_3 and Ag layer thickness oscillations (the SiO_x substrate being unresolved). The low frequency oscillations are clearly more damped in sample S1, indicating a higher interface roughness. The deduced structural parameters of samples S1–S3 are listed in Table I. The structural data for intermediate evaporation rates fall into these extreme values. Interestingly, the surface roughness in S1 (slowest deposition rate) is found to be 1.7 times higher than in S2 (highest deposition rate). From the electron density profiles in Figure 1(b), the electron density of the silver layer in S1 is found to be 6% lower compared to S2 or bulk silver, indicating that a slower deposition rate leads to a rougher and slightly more porous metal layer. The Alq_3/Ag interface roughness (σ_{Alq3}) is found to be weakly dependent

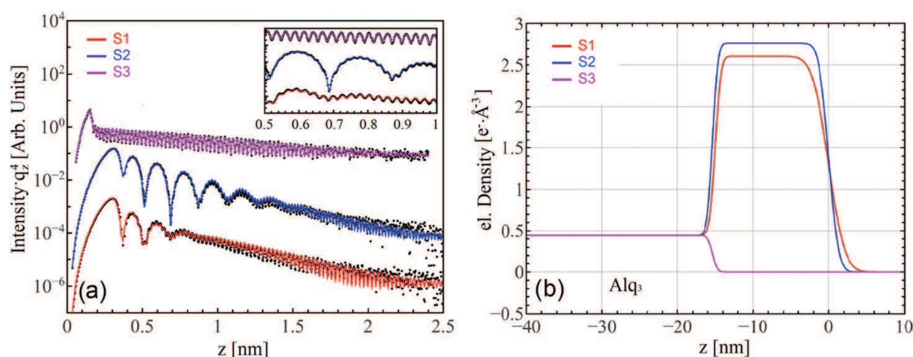

FIG. 1. (a) XRR characterization of samples described in Table I. The simulations for S1 and S2 based on a three-layer model (two for S3) are shown by continuous lines. Data have been vertically shifted for helping the comparison. The inset shows a magnified view of the XRR thickness oscillations in the indicated q_z interval. (b) Electron density profiles (S1 in red, S2 in blue, and S3 in magenta line) along the vertical direction z as derived from the best fit parameters of the XRR data.

[This article is copyrighted as indicated in the article. Reuse of AIP content is subject to the terms at: http://scitation.aip.org/termsconditions. Downloaded to] IP: 134.2.182.197 On: Mon, 24 Aug 2015 09:08:18

TABLE I. Electron density (ρ) and surface roughness (σ) of Ag (15 nm)/Alq_3($\sim$150 nm)/SiO_x hybrid layers resulting from the simulation of the X-ray specular reflectivity data shown in Figure 1.

Sample, structure	Ag evap. rate (Å/s)	Ag		Alq_3	
		ρ (Å^{-3})	σ (nm)	ρ (Å^{-3})	σ (nm)
S1, Ag/Alq_3/SiO_x	0.2	2.61 ± 0.09	1.7 ± 0.2	0.44 ± 0.09	0.59 ± 0.03
S2, Ag/Alq_3/SiO_x	10	2.77 ± 0.08	1.00 ± 0.05	0.44 ± 0.09	0.57 ± 0.02
S3, Alq_3/SiO_x	…	…	…	0.42 ± 0.04	0.50 ± 0.01

from the evaporation conditions, being only 18% higher than the surface roughness of a bare Alq_3 layer. This suggests that a modest (homogeneous) silver diffusion occurs during the evaporation process.[42] On the other hand, by lowering of the deposition rate, a proportional decrease in the Ag density is observed. This suggests that silver diffusion does not take place along a laterally averaged diffusion profile, as modeled by Fick's law, but it rather involves a localized diffusion along statistically distributed paths. This local diffusion results to be stronger for slow deposition rates.

B. Memory devices characteristics

Figure 2(a) shows the typical I-V curves obtained after the forming step: at a low read-out voltage, stable high and low resistance states (HRS and LRS) are observed. At the threshold voltage, typically occurring between 2.5 and 3.5 V, the device switches from its HRS to its LRS which corresponds to the memory set. The threshold is followed by a negative differential resistance (NDR) region where the current decreases while increasing the bias. A voltage pulse applied at the end of the NDR region sets the device back into its HRS (erase voltage). It has been already shown that, by applying a bias value within the NDR region, it is possible to program non-volatile intermediate resistance states between the HRS and LRS.[6,8] The same behavior was clearly observed in our single layered memory device (Figure 2(a)), therefore allowing for multi-bit storing. In addition, Figure 2(b) shows the reliability and endurance of such a basic memory device during a cycling test. The cycle consists of the subsequent application of the identified 1s bias pulses, namely, the write (+3 V), read (+1 V), erase (+6.5 V), and read voltages. Although some variations of the absolute current levels can be observed in the HRS, a clear discrimination between states is always obtained. The HRS variation can be well explained based on our interpretation of the switching mechanism and will be discussed later. The retention time of the devices has been tested by repeated measurements in different devices in different conductive states over time, and no change of the individual state has been observed over a test period of 2 yr. Hence, it is fair to state that a retention time longer than 2 yr may be assigned.

C. Depth profile analysis

The compositional changes induced by I-V testing have been monitored by comparing the XPS depth profiles of silver, carbon, and indium in as-deposited (Figure 3(a)) and electrically addressed (Figures 3(b) and 3(c)) memory elements. Starting from a depth of about 50 nm under the Alq_3/Ag interface, the atomic percentage of silver with respect to carbon drops to about 0.01%; an accurate peak fitting procedure of the Ag3d doublet was necessary to identify such a weak XPS signal corresponding to a surface density of about 10^{11} atoms/cm^2 or, equivalently, to an average bulk doping of $\sim 5 \times 10^{18}$ at/cm^3. Silver and indium (opposite) diffusion is found to be slightly enhanced by the I-V cycling; however, quantification, imaging, or chemical analysis were not possible with such low signals. Interestingly, a higher oxygen content ($O_{at.\%} > 4\%$) is found in the Alq3 layer in cycled devices with respect to the pristine one ($O_{at.\%} < 3\%$). The very low oxide component in the Ag3d high resolution

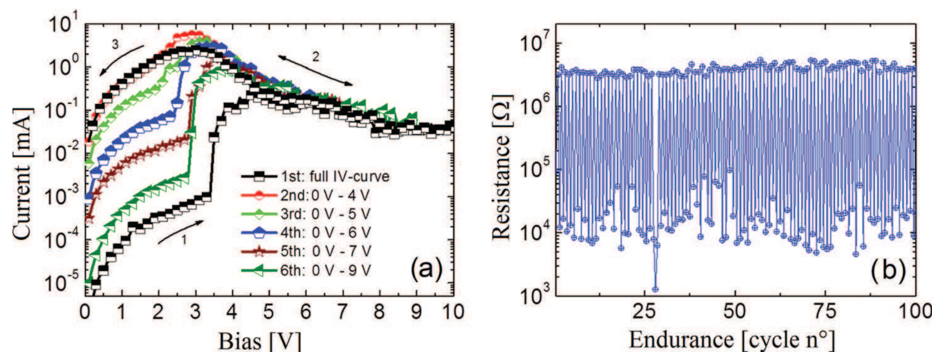

FIG. 2. I-V characteristics and switching endurance test of ITO/Alq_3/Ag devices. (a) Sequential unipolar I-V sweeps; a sharp current threshold switches the device from its starting HRS to its LRS (write process at 3.5 ± 0.5 V). Subsequently, a negative differential resistance (NDR) region can be found. Applying a bias within the NDR region, multiple N-V intermediate resistance states are addressed, while a bias at the end of this NDR region switches the device to its starting HRS (erase process at 10 V). When going from 10 to 0 V, the device goes back to the LRS. At a reading bias (1.5 V) well below the current threshold, the resistance can be safely read without influencing the device state. (b) Typical endurance test of a device obtained by writing, reading, erasing, and reading again the memory state. The resistance states at the reading bias are displayed as a function of the cycle number.

[This article is copyrighted as indicated in the article. Reuse of AIP content is subject to the terms at: http://scitation.aip.org/termsconditions. Downloaded to] IP: 134.2.182.197 On: Mon, 24 Aug 2015 09:08:18

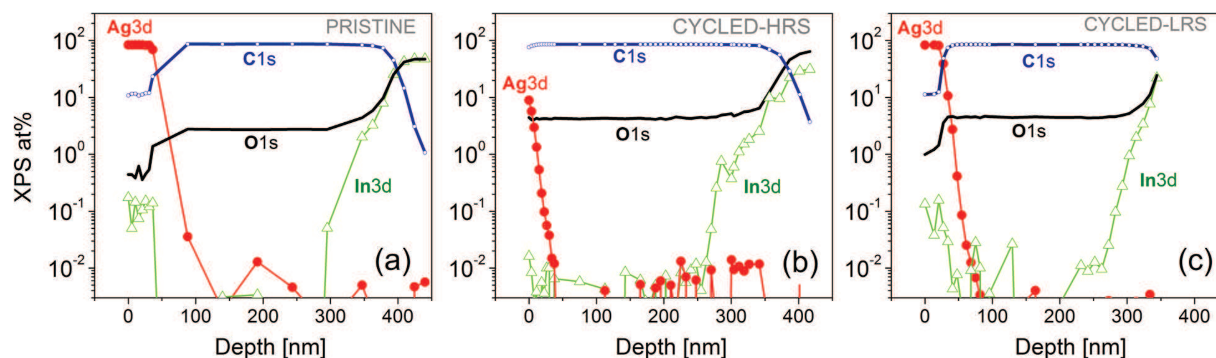

FIG. 3. XPS depth profile analysis of ITO/Alq_3/Ag memory elements. Silver (Ag3d), carbon (C1s), oxygen (O1s), and indium (In3d) atomic percentages (log scale) are shown as a function of the sputtering depth. The memory devices were as-deposited (a), or set after few cycles in the HRS (b), or in the LRS (c).

spectra suggests that the oxygen diffusion comes from the ITO layer.

Dual beam ToF-SIMS 3D analysis is carried on pristine and cycled memory elements allowing for a higher sensitivity and spatial resolution. 3D reconstructions are built from the 2D images of the full mass spectrum acquired at each profile step. Molecular ions can be subsequently selected from the mass spectrum and their 3D distribution can be displayed within the total analysis volume. In particular, $Ag^{(-)}$ XY maps can be built by integrating, and projecting on the XY plane, the $Ag^{(-)}$ 2D images acquired through the whole depth profile. Silver XY maps are shown in Figure 4 for a pristine (Figure 4(a)) and electrically addressed memories (Figures 4(b) and 4(c)). Multiple micron-size spots of distributed intensities can be identified, indicating regions where a localized (filamentary) silver diffusion occurred. Cross section reconstructions along YZ direction are shown in Figures 5(a)–5(c). It allows to visually evaluating the $Ag^{(-)}$ diffusion depth in the filament region (the YZ cuts are indicated by the vertical lines in Figure 4). Interestingly, for the most intense spots, the Ag diffusion is found to extend almost till the bottom electrode with fairly similar intensities. A closer look at the CF region in as-deposited, cycled-LRS and cycled-HRS devices allowed for identifying what we interpreted as pre-filaments, inactivated filaments, and a possibly active filament. This is shown by the profile reconstructions in Figure 5. ToF-SIMS being a semi-quantitative analysis, the signals in the profiles have been normalized to the $Ag^{(-)}$ intensity on the top electrode in order to more easily compare the profiles obtained in the different samples/states. In as-deposited memory elements, almost complete (pre-) filaments are found to extend up to 200 nm beneath the Alq_3/Ag interface, leaving a small gap between the end of the silver tip, acting as a virtual cathode, and the ITO bottom electrode (Figures 5(a) and 5(d)). In cycled devices, the most intense spots correspond to CFs clearly reaching the bottom electrode. The Ag signal measured in the ITO layer (Figures 5(b) and 5(e)) is likely to be amplified by the presence of the oxygen rich matrix and by a possible higher Cs implantation; both effects are well known to enhance the ionization yield of negative ion species. In cycled-HRS devices, those CFs are always characterized by a significant drop on the $Ag^{(-)}$ intensity close to the Ag/Alq_3 interface suggesting that a local breakdown of the CF occurred (Figures 5(b) and 5(e)). The local increase of the signals intensities from oxygen, sulfur, and the molecular ion identified with silver oxide/sulfide ($AgSO^{(-)}$ and $AgO_3^{(-)}$ at 155 amu) points towards a filament inactivation process associated with a local oxidation of the CF. In the ToF-SIMS, profile silver from AgO contributes to the overall $Ag^{(-)}$ intensity which is measured in the breakdown region. To our knowledge, this is the first experimental evidence of CF inactivation mechanism in organic memories. In inorganic memories, CF growth and erase have been recently directly observed by AFM tomography and by TEM on planar devices.[43–45] In the cycled-LRS device, we could identify a slightly lower intense CF not showing any

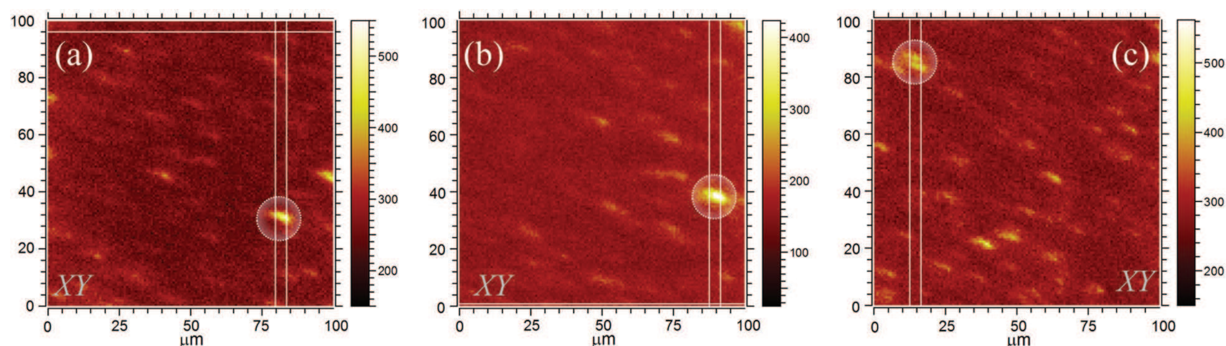

FIG. 4. ToF-SIMS $Ag^{(-)}$ XY maps on ITO/Alq_3/Ag memories. Panel (a) refers to a memory as-deposited, (b) to a cycled-HRS, and (c) to a cycled-LRS. The high intensity spots indicate areas of silver diffusion which can be visualized in the YZ reconstructions in Figure 5. XY maps can also be used to select the filament region and successively reconstruct the ToF-SIMS depth profile of proper molecular ions in the selected volume.

[This article is copyrighted as indicated in the article. Reuse of AIP content is subject to the terms at: http://scitation.aip.org/termsconditions. Downloaded to] IP: 134.2.182.197 On: Mon, 24 Aug 2015 09:08:18

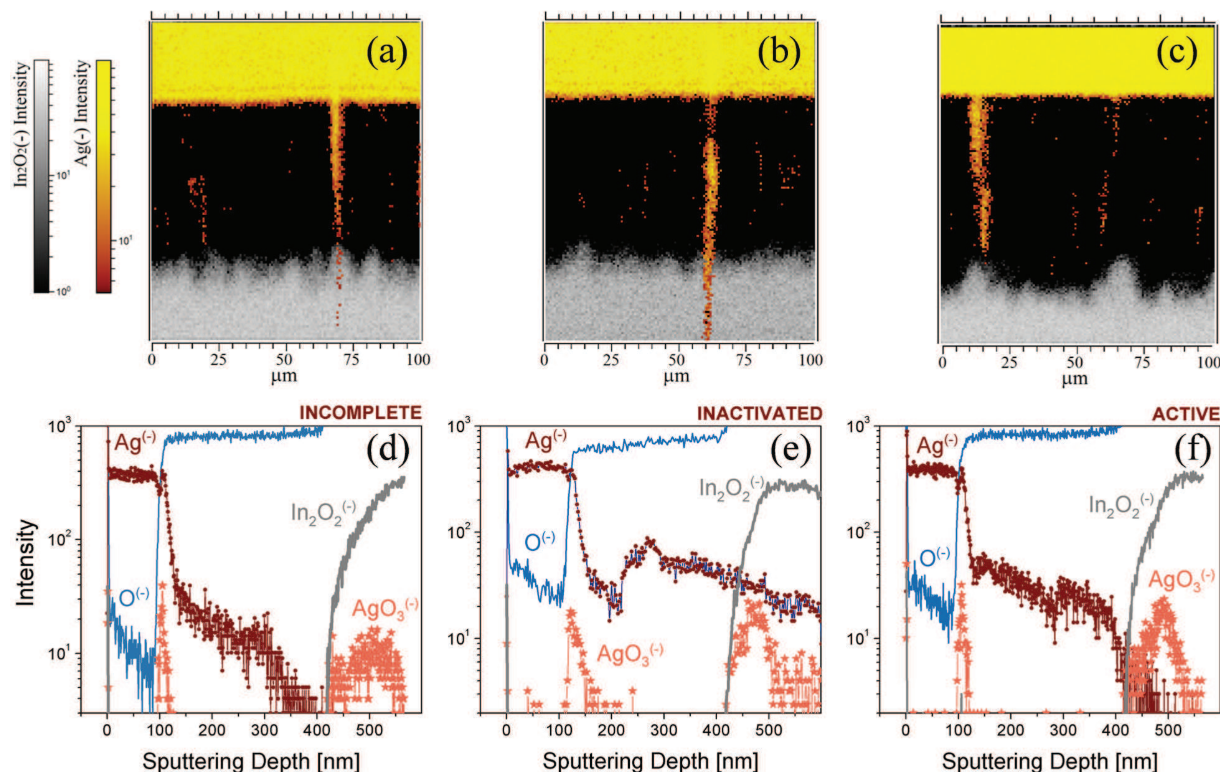

FIG. 5. ToF-SIMS 3D imaging of ITO/Alq_3/Ag memory elements. The YZ cross section reconstruction (indicated in Figure 4) shows the distribution of $Ag^{(-)}$ (top electrode) and $In_2O_2^{(-)}$) (ITO) on CF region in as-deposited (a), cycled-HRS (b), and cycled-LRS (c) memory elements. Panels (d)–(f) are the normalized depth profiles reconstructions in the CF region (as indicated in Figure 4). Oxygen and silver oxide/sulfide ($AgO_3^{(-)}$ and $AgSO^{(-)}$ peaks are not separated) are displayed to visualize metal oxidation. The oxidation and drop of the Ag signal at the Ag/Alq_3 interface (panel (e)) are interpreted as an indication for filament breakdown.

significant drop of the $Ag^{(-)}$ signal. The absence of a drop in the Ag profile and the absence of peaks related to AgO are considered as a good indication for a connected/active CF. It has been shown that in a multi metal island system, the LRS can be sustained by tunneling through islands separated by 2–5 nm gaps.[44] Concerning the CF section, a close look to the filament region indicates a radial distribution of $Ag^{(-)}$; this points towards an effective filament section smaller than our in-plane resolution ($\sim 1 \times 1\ \mu m^2$) in agreement with the very low Ag at. % measured with XPS. Finally, the abundance of $Ag^{(-)}$ spots visible in the integrated XY maps, with distributed intensities, suggest that the conductivity in the LRS state may be supported by a distribution of CFs (with distributed resistivities) which are successively activated by metal drift through the small gap between the Ag virtual cathodes and the bottom electrode. However, the formation of a continuous metal path through which most of the current would flow limits the formation of other fully connected CF and justifies the very low variability of the LRS current which is observed in the cycling test. When biasing the devices in the post-threshold region, starting from highest conductive paths, CFs are suggested to undergo local electrochemical breakdown (associated with the drift of the oxygen and sulfur), giving rise to the NDR behaviour. In principle, low-conducting paths could be established when biasing in the post-threshold (NDR) region, so that a dynamic equilibrium between the CFs which are formed and ruptured is established.[46] At the end of the NDR region, CFs cannot anymore sustain the current which flows only through isolated metal islands within the organic layer. The high device endurance suggests that the same conductive path is possibly recovered at the subsequent cycle, as soon as charges released at the filament breakdown are relaxed.

IV. CONCLUSIONS

Metal diffusion is investigated in hybrid Alq_3/Ag films and in ITO/Alq_3/Ag organic resistive memories. XRR analysis allowed correlating the evaporation conditions to the morphology of hybrid layers, showing that the interfaces are abrupt and the average diffusion of silver is weakly dependent from the evaporation rate (in the considered range); however, the presence of inhomogeneous diffusion is suggested by the decrease in the metal porosity which is observed at lower evaporation rate; this interesting fact indicates that the evaporation rate is likely to influence the switching behavior, in particular, the forming step and the resistivity in the HRS; we think that a systematic study on this phenomenon would be highly desirable; however, it is beyond the scope of the present work. ITO/Alq_3/Ag organic memories displaying regular unipolar bistable I-V characteristics and multi-bit storage capability have been characterized. In particular, programming capability with pulsed biasing was demonstrated in an endurance cycling test. Thanks to their very basic structure, consisting of only few chemical components, such devices were ideal candidates for the combined XPS and

[This article is copyrighted as indicated in the article. Reuse of AIP content is subject to the terms at: http://scitation.aip.org/termsconditions. Downloaded to] IP: 134.2.182.197 On: Mon, 24 Aug 2015 09:08:18

ToF–SIMS analyses. ToF-SIMS 3D imaging was performed on as-deposited devices showing the presence of *ready-to-switch* silver pre-filaments extending up to 200 nm in the Alq_3 layer. In our interpretation, the significant variability of the HRS conductivity relies on a conduction mechanism based on tunneling through multiple disconnected metal islands paths, on the other hand, in the LRS, one (or few) fully bridged CFs provide an ohmic path between the electrodes. In the NDR region, a local breakdown/oxidation of the CF occurs and a dynamic equilibrium may be established between the ruptured and formed CFs with distributed resistivities. Our results and interpretation are in close agreement with what has been recently observed in inorganic memoristors in which the NDR behaviour is explained by a process progressive degradation of (large) CFs.[44] This work clearly demonstrates the high potential of depth profile techniques for the characterization of CFs in resistive switching memory stacks. Given the similarity, we suggest that CFs formation should also be taken into account when designing light emitting and photovoltaic organic electronic devices based on metallized thin organic layers.

ACKNOWLEDGMENTS

We acknowledge the financial support from the FP7-NMP-2010-SMALL-4 program, Project No. 263073 (HYMEC).

[1]W.-P. Lin, S.-J. Liu, T. Gong, Q. Zhao, and W. Huang, Adv. Mater. **26**, 570 (2014).
[2]T. W. Kim, Y. Yang, F. Li, and W. L. Kwan, NPG Asia Mater. **4**, e18 (2012).
[3]S. Nau, C. Wolf, S. Sax, and E. J. W. List-Kratochvil, Adv. Mater. **27**, 1048 (2015).
[4]P.-T. Lee, T.-Y. Chang, and S.-Y. Chen, Org. Electron. **9**, 916 (2008).
[5]K. Onlaor, B. Tunhoo, T. Thiwawong, and J. Nukeaw, Curr. Appl. Phys. **12**, 331 (2012).
[6]J.-G. Park, W.-S. Nam, S.-H. Seo, Y.-G. Kim, Y.-H. Oh, G.-S. Lee, and U.-G. Paik, Nano Lett. **9**, 1713 (2009).
[7]D. Prime and S. Paul, Philos. Trans. R. Soc., A **367**, 4141 (2009).
[8]S. Nau, S. Sax, and E. J. W. List-Kratochvil, Adv. Mater. **26**, 2508 (2014).
[9]A. C. Dürr, N. Koch, M. Kelsch, A. Rühm, J. Ghijsen, R. Johnson, J.-J. Pireaux, J. Schwartz, F. Schreiber, H. Dosch, and A. Kahn, Phys. Rev. B **68**, 115428 (2003).
[10]A. C. Duürr, F. Schreiber, M. Kelsch, H. D. Carstanjen, H. Dosch, and O. H. Seeck, J. Appl. Phys. **93**, 5201 (2003).
[11]A. C. Dürr, F. Schreiber, M. Kelsch, H. D. Carstanjen, and H. Dosch, Adv. Mater. **14**, 961 (2002).
[12]J. H. Cho, D. H. Kim, Y. Jang, W. H. Lee, K. Ihm, J.-H. Han, S. Chung, and K. Cho, Appl. Phys. Lett. **89**, 132101 (2006).
[13]M. Scharnberg, R. Adelung, and F. Faupel, Phys. Status Solidi **205**, 578 (2008).
[14]A. K. Mahapatro, R. Agrawal, and S. Ghosh, J. Appl. Phys. **96**, 3583 (2004).
[15]N. Koch, A. C. Dürr, J. Ghijsen, R. L. Johnson, J.-J. Pireaux, J. Schwartz, F. Schreiber, H. Dosch, and A. Kahn, Thin Solid Films **441**, 145 (2003).
[16]M. L. Wang, J. Zhou, X. D. Gao, B. F. Ding, Z. Shi, X. Y. Sun, X. M. Ding, and X. Y. Hou, Appl. Phys. Lett. **91**, 143511 (2007).
[17]P. Sebastian, F. Lindner, K. Walzer, B. Luüssem, and K. Leo, J. Appl. Phys. **110**, 084508 (2011).
[18]S. Gao, F. Zeng, C. Chen, G. Tang, Y. Lin, Z. Zheng, C. Song, and F. Pan, Nanotechnology **24**, 335201 (2013).
[19]Y. T. You, Q. Zeng, Y. Yao, M. L. Wang, B. Wu, Y. He, Y. M. Hu, C. Q. Wu, and X. Y. Hou, Appl. Phys. Lett. **100**, 123304 (2012).
[20]Y. Yang, P. Gao, L. Li, X. Pan, S. Tappertzhofen, S. Choi, R. Waser, I. Valov, and W. D. Lu, Nat. Commun. **5**, 4232 (2014).
[21]L. D. Bozano, B. W. Kean, V. R. Deline, J. R. Salem, and J. C. Scott, Appl. Phys. Lett. **84**, 607 (2004).
[22]V. S. Reddy, S. Karak, and A. Dhar, Appl. Phys. Lett. **94**, 173304 (2009).
[23]J. Lin and D. Ma, J. Appl. Phys. **103**, 124505 (2008).
[24]L. D. Bozano, B. W. Kean, M. Beinhoff, K. R. Carter, P. M. Rice, and J. C. Scott, Adv. Funct. Mater. **15**, 1933 (2005).
[25]B. Jiao, Z. Wu, H. Dong, S. Ning, and X. Hou, J. Phys. D: Appl. Phys. **46**, 445107 (2013).
[26]M. Lauters, B. McCarthy, D. Sarid, and G. E. Jabbour, Appl. Phys. Lett. **87**, 231105 (2005).
[27]W.-J. Joo, T.-L. Choi, K.-H. Lee, and Y. Chung, J. Phys. Chem. B **111**, 7756 (2007).
[28]T.-W. Kim, S.-H. Oh, H. Choi, G. Wang, H. Hwang, D.-Y. Kim, and T. Lee, Appl. Phys. Lett. **92**, 253308 (2008).
[29]Y. Ji, M. Choe, B. Cho, S. Song, J. Yoon, H. C. Ko, and T. Lee, Nanotechnology **23**, 105202 (2012).
[30]U. S. Bhansali, M. A. Khan, D. Cha, M. N. Almadhoun, R. Li, L. Chen, A. Amassian, I. N. Odeh, and H. N. Alshareef, ACS Nano **7**, 10518 (2013).
[31]B. Cho, J.-M. Yun, S. Song, Y. Ji, D.-Y. Kim, and T. Lee, Adv. Funct. Mater. **21**, 3976 (2011).
[32]C. Pearson, L. Bowen, M.-W. Lee, A. L. Fisher, K. E. Linton, M. R. Bryce, and M. C. Petty, Appl. Phys. Lett. **102**, 213301 (2013).
[33]Y. C. Yang, F. Pan, Q. Liu, M. Liu, and F. Zeng, Nano Lett. **9**, 1636 (2009).
[34]R. Waser, Microelectron. Eng. **86**, 1925 (2009).
[35]J. Chen, C. Hsin, C. Huang, C. Chiu, Y. Huang, S.-J. Lin, W.-W. Wu, and L.-J. Chen, Nano Lett. **13**, 3671 (2013).
[36]U. Celano, L. Goux, A. Belmonte, K. Opsomer, A. Franquet, A. Schulze, C. Detavernier, O. Richard, H. Bender, M. Jurczak, and W. Vandervorst, Nano Lett. **14**, 2401 (2014).
[37]K. J. Yoon, M. H. Lee, G. H. Kim, S. J. Song, J. Y. Seok, S. Han, J. H. Yoon, K. M. Kim, and C. S. Hwang, Nanotechnology **23**, 185202 (2012).
[38]Y. Busby, N. Crespo-Monteiro, M. Girleanu, M. Brinkmann, O. Ersen, and J. Pireaux, Org. Electron. **16**, 40 (2015).
[39]G. Casula, P. Cosseddu, Y. Busby, J.-J. Pireaux, M. Rosowski, B. Tkacz Szczesna, K. Soliwoda, G. Celichowski, J. Grobelny, J. Novák, R. Banerjee, F. Schreiber, and A. Bonfiglio, Org. Electron. **18**, 17 (2015).
[40]N. Wehbe, J.-J. Pireaux, and L. Houssiau, J. Phys. Chem. C **118**, 26613 (2014).
[41]M. Björck and G. Andersson, J. Appl. Crystallogr. **40**, 1174 (2007).
[42]W. Xu, J. Brauer, G. Szulczewski, M. Sky Driver, and A. N. Caruso, Appl. Phys. Lett. **94**, 233302 (2009).
[43]U. Celano, L. Goux, A. Belmonte, K. Opsomer, R. Degraeve, C. Detavernier, M. Jurczak, and W. Vandervorst, J. Phys. Chem. Lett. **6**, 1919 (2015).
[44]H. Sun, Q. Liu, C. Li, S. Long, H. Lv, C. Bi, Z. Huo, L. Li, and M. Liu, Adv. Funct. Mater. **24**, 5679 (2014).
[45]Y. Yang, P. Gao, S. Gaba, T. Chang, X. Pan, and W. Lu, Nat. Commun. **3**, 732 (2012).
[46]G. Dearnaley, D. V. Morgan, and A. M. Stoneham, J. Non-Cryst. Solids **4**, 593 (1970).

[This article is copyrighted as indicated in the article. Reuse of AIP content is subject to the terms at: http://scitation.aip.org/termsconditions. Downloaded to] IP: 134.2.182.197 On: Mon, 24 Aug 2015 09:08:18